

Structural and thermodynamic properties of inhomogeneous fluids in rectangular corrugated nano-pores

Yanshuang Kang(康艳霜), Haijun Wang(王海军), and Zongli Sun(孙宗利)
Citation: Chin. Phys. B, 2022, 31 (**5**): 056104. DOI: 10.1088/1674-1056/ac4237
Journal homepage: http://cpb.iphy.ac.cn; http://iopscience.iop.org/cpb

What follows is a list of articles you may be interested in

Probing structural and electronic properties of divalent metal Mg_{n+1} and $SrMg_n$ (n = 2–12) clusters and their anions

Song-Guo Xi(奚松国), Qing-Yang Li(李青阳), Yan-Fei Hu(胡燕飞), Yu-Quan Yuan(袁玉全), Ya-Ru Zhao(赵亚儒), Jun-Jie Yuan(袁俊杰), Meng-Chun Li(李孟春), and Yu-Jie Yang(杨雨杰)
Chin. Phys. B, 2022, 31 (**1**): 016106. DOI: 10.1088/1674-1056/ac04aa

First-principles study of structural and opto-electronic characteristics of ultra-thin amorphous carbon films

Xiao-Yan Liu(刘晓艳), Lei Wang(王磊), and Yi Tong(童祎)
Chin. Phys. B, 2022, 31 (**1**): 016102. DOI: 10.1088/1674-1056/ac0cd8

Band alignment in SiC-based one-dimensional van der Waals homojunctions

Xing-Yi Tan(谭兴毅), Lin-Jie Ding(丁林杰), and Da-Hua Ren(任达华)
Chin. Phys. B, 2021, 30 (**12**): 126102. DOI: 10.1088/1674-1056/abfbd2

A novel two-dimensional SiO sheet with high-stability, strain tunable electronic structure, and excellent mechanical properties

Shijie Liu(刘世杰) and Hui Du(杜慧)
Chin. Phys. B, 2021, 30 (**7**): 076104. DOI: 10.1088/1674-1056/abf34d

Novel rubidium polyfluorides with F_3, F_4, and F_5 species

Ziyue Lin(林子越), Hongyu Yu(于洪雨), Hao Song(宋昊), Zihan Zhang(张子涵), Tianxiao Liang(梁天笑), Mingyang Du(杜明阳), and Defang Duan(段德芳)
Chin. Phys. B, 2021, 30 (**6**): 066102. DOI: 10.1088/1674-1056/abefc6

Structural and thermodynamic properties of inhomogeneous fluids in rectangular corrugated nano-pores

Yanshuang Kang(康艳霜)[1,2], Haijun Wang(王海军)[1,3,4,†], and Zongli Sun(孙宗利)[5,‡]

[1] *College of Chemistry and Environmental Science, Hebei University, Baoding* 071002, *China*
[2] *College of Science, Hebei Agricultural University, Baoding* 071001, *China*
[3] *Chemical Biology Key Laboratory of Hebei Province, Hebei University, Baoding* 071002, *China*
[4] *Key Laboratory of Medicinal Chemistry and Molecular Diagnosis, Ministry of Education, Hebei University, Baoding* 071002, *China*
[5] *Department of Mathematics and Physics, North China Electric Power University, Baoding* 071003, *China*

(Received 6 September 2021; revised manuscript received 24 November 2021; accepted manuscript online 11 December 2021)

Based on the free-energy average method, an area-weighted effective potential is derived for rectangular corrugated nano-pore. With the obtained potential, classical density functional theory is employed to investigate the structural and thermodynamic properties of confined Lennard–Jones fluid in rectangular corrugated slit pores. Firstly, influence of pore geometry on the adsorptive potential is calculated and analyzed. Further, thermodynamic properties including excess adsorption, solvation force, surface free energy and thermodynamic response functions are systematically investigated. It is found that pore geometry can largely modulate the structure of the confined fluids, which in turn influences other thermodynamic properties. In addition, the results show that different geometric elements have different influences on the confined fluids. The work provides an effective route to investigate the effect of roughness on confined fluids. It is expected to shed light on further understanding about interfacial phenomena near rough walls, and then provide useful clues for the design and characterization of novel materials.

Keywords: free-energy average, rectangular corrugated pore, density functional

PACS: 61.20.Gy, 62.10.+s **DOI:** 10.1088/1674-1056/ac4237

1. Introduction

Fluids in restricted geometry have unique structures and thermodynamic properties,[1,2] which differ significantly from those of bulk phase. The confined fluids are so ubiquitous that they have obtained a wide spectrum of practical applications in technological and engineering fields, such as catalysis,[3,4] membrane separations,[5] heat exchange,[6] carbon capture and storage.[7–9] In addition, the interplay of finite size effect and surface effect in confined fluid can strongly modulate its phase behaviors,[10,11] and even rheological properties.[12–14] These distinctive properties of confined fluid make it rather fascinating and interesting.

In the past decades, confined fluid have been investigated by using of a variety of theoretical methods. Employed density functional theory (DFT), Peng *et al.*[15] investigated the adsorption of nitrogen in MCM-41 material, which is modelled by a cylindrical pore. Sun *et al.*[16] studied the pressure tensor of inhomogeneous Lennard–Jones (LJ) fluids in spherical cavity. With the calculated pressure components, solid–fluid interfacial tension had also been studied. By solving the Ornstein–Zernike equation, density profiles of fluids inside slit, spherical and cylindrical pores had been studied by Zhou *et al.*[17–19] In addition to density profile, the partition coefficient and solvation force of the confined fluids were also investigated. In addition, computer simulations[20] are frequently employed to investigate confined fluids. By utilizing of grand ensemble Monte–Carlo (GCMC) simulation, Peterson *et al.*[21] studied the adsorption isotherm and phase transition of LJ fluid confined in cylindrical pore. Performing molecular dynamics (MD) simulations, Magda *et al.*[22] studied density profiles, solvation forces, interfacial tensions and self-diffusion coefficients of confined LJ fluid. Despite so many investigations about the confined fluids, most of them focus on planar, spherical or cylindrical pores, because these simple geometries can be easily modelled. Nevertheless, these pores may be markedly different from real materials, whose surfaces are usually rough on an atomic scale. This has been confirmed by some recent studies on gas adsorption on some specific adsorbents.[23–25]

Prior to investigating the effect of roughness on the confined fluids, the solid–fluid potential near walls should be firstly determined. In their simulation of gases on an infinite set of straight square-walled grooves, Bojan and Steele[26] (BS) obtained the solid–liquid potential by summing up the LJ pair interactions between one fluid atom and the solid. In addition, Schoen *et al.* had calculated the solid–fluid potential of chemically[27,28] and geometrically[29,30] heterogeneous slit pores in their investigation of the ultrathin fluid film. Following the BS method, Wu *et al.* derived coarse-grained potentials arising from patterned cylindrical or rectan-

†Corresponding author. E-mail: whj@hbu.edu.cn
‡Corresponding author. E-mail: sunzl@ncepu.edu.cn

© 2022 Chinese Physical Society and IOP Publishing Ltd

gular pillars,[31] as well as that from rectangular grooves.[32] The obtained potentials were further used in their MD simulations to probe the wetting of LJ liquid droplet on various patterned solid surfaces. Recently, Liu *et al.*[33] developed a general method to calculate the averaged solid–fluid potential energies for a wide range of adsorbent models with different extension and shape. By direct integration over the pair potential between the fluid and solid atoms, Malijevský calculated the solid–fluid potential of solid grooved substrates.[34–38] Based on the obtained potential, a series of interfacial phenomena including filling,[34] wetting,[35] bridging,[36] interface pinning,[37] capillary contact angle, and condensation–evaporation transitions[38] had been investigated.

Though explicit results of solid–liquid potential are readily available for rough surfaces, their applications in either DFT or computer simulation may be strenuous because of the involved multi-dimension. For example, by performing a 2-dimensional nonlocal density functional theory (2D-NLDFT), Jagiello *et al.*[39–41] investigated the pore size distribution of adsorbents through calculation of the adsorption isotherms in rough pores. Moreover, Yatsyshin *et al.*[42,43] had also performed 2D-NLDFT calculations in their investigations of wetting and capillary condensation near corrugated walls. Actually, efforts have been made to simplify the DFT calculation near rough surfaces. One representative may be the quenched solid density functional theory (QSDFT),[44,45] which models the solid by the density distribution of solid atoms in the direction perpendicular to the surface rather than the source of the external potential. Besides, combining the theories of Markovian random processes and the first passage time probability, Aslyamov *et al.*[46,47] obtained an effective solid–fluid potential for heterogeneous surfaces, with which a random surface density functional theory (RSDFT) has been developed.

Recently, Forte *et al.*[48] found that the widely employed integrated potentials, such as Steele 10–4–3 potential, are only the leading-order terms in the high-temperature expansion of an original free-energy-averaged (O-FEA) solid–fluid potential. They argued that for surfaces with irregular geometrical defects, the temperature-dependent FEA potential should be more preferable. Actually, the FEA procedure provides an useful way to obtain the effective solid–fluid potentials, whose efficiency has been verified in calculations for the rough surfaces.[49] In a very recent work of Shi *et al.*,[50] a bottom-up strategy was proposed, and the effective pore potential was calculated via a random-configuration area-weighted free-energy-average (RC-AW-FEA) operation. This routine shows remarkable superiority over the O-FEA. However, it is not suitable for the conventional DFT calculation because of the involved random-configuration sampling. In order to extend the AW-FEA method to DFT calculations for fluid near rough surface, we aim to derive a 1-dimensional effective solid–fluid potential, with which the fluids confined in rough pore can be conveniently calculated.

This paper is organized as follow. In Section 2, a mean-field AW-FEA potential model is proposed to calculate the effective solid–fluid potential in the rectangular corrugated slit pore. In Section 3, the framework of DFT and some approximations for free energy functional of confined fluids are given. In Section 4, the structural and thermodynamic properties of confined LJ fluids in rectangular corrugated slit pores are investigated. The effects of pore geometry on these properties are analyzed in detail. In the final section, a short summary is given.

2. Mean-field AW-FEA model

The present work considers a rectangular corrugated slit pore, which is composed of two identical rectangular corrugated substrates, as sketched in Fig. 1(a). Each corrugated substrate can be regarded as the sum of a basal planar wall and an infinite set of parallel and identical pillars. These pillars are equidistantly distributed along y-direction with a spatial period $\lambda = w_1 + w_2$. Note that both corrugated substrates are infinitely extended in x- and y-directions.

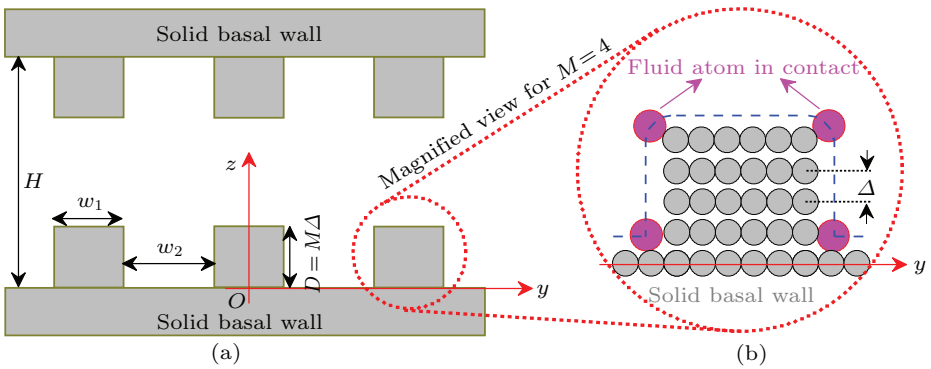


Fig. 1. (a) Cross sectional view of the rectangular corrugated slit pore. w_1, w_2 and $D = M\Delta$ specify the geometry of pillars. M denotes the number of layers in each pillar, while Δ is the interlayer spacing. (b) Magnified view of the pillar structure (gray) in the case of $M = 4$. The magenta balls represent test fluid atoms in contact with the pillar, and the dashed line denotes the boundary of the accessible space around one pillar. Note that in (b), the size of balls of different species does not reflect the real size of the corresponding atom.

The solid–fluid and fluid–fluid interactions are described by the LJ potential

$$\varphi_{ij}(r) = 4\varepsilon_{ij}\left[\left(\frac{\sigma_{ij}}{r}\right)^{12} - \left(\frac{\sigma_{ij}}{r}\right)^{6}\right] \tag{1}$$

with subscripts $i, j = \mathrm{s,f}$. ε_{ij} and σ_{ij} are respectively energy and size parameters, which satisfy the Lorentz mixing rules. For the sake of concise, σ_{ff} and $\varepsilon_{\mathrm{ff}}$ are abbreviated as σ and ε, respectively. Other lengths and energies are measured in unit of σ and ε, respectively. Note that in calculation of the effective potential via the AW-FEA, one should keep in mind the accessible region of the fluid atom. To this end, the sketch of boundary of the accessible space around one pillar has been presented in Fig. 1(b).

The potential arising from the basal planar wall is modelled by the Steele 10–4–3 potential[51]

$$V_{\mathrm{St}}(z) = 2\pi\varepsilon_{\mathrm{fs}}\rho_{\mathrm{St}}\sigma_{\mathrm{fs}}^2\Delta\left[\frac{2}{5}\left(\frac{\sigma_{\mathrm{fs}}}{z}\right)^{10} - \left(\frac{\sigma_{\mathrm{fs}}}{z}\right)^{4} - \frac{\sigma_{\mathrm{fs}}^4}{3\Delta\,(z+0.61\Delta)^3}\right] \tag{2}$$

with ρ_{St} being the volumetric density of solid atoms. Assume that each pillar consists of M atomic layers in z-direction. Therefore, for a test fluid atom locating at (y,z), the potential from one single corrugated substrate can be expressed as

$$V_{\mathrm{subs}}(y,z) = V_{\mathrm{St}}(z) + \sum_{n=-\infty}^{+\infty}\sum_{m=1}^{M} V_{m,n}(y,z), \tag{3}$$

where $V_{m,n}(y,z)$ is the potential contributed from the m-th atomic layer in the n-th pillar. The index m and n are used to distinguish the solid layers and pillars, respectively. Actually, due to the translational symmetry along y-direction, one should only calculate the potential from the 0-th pillar, say $V_0(y,z)$, while those from other pillars can be simply obtained by spatial translation along y-direction. Therefore, $V_{\mathrm{subs}}(y,z)$ can be rewritten as

$$V_{\mathrm{subs}}(y,z) = V_{\mathrm{St}}(z) + \sum_{n=-\infty}^{+\infty}\sum_{m=1}^{M} V_{m,0}(y+n\lambda,z) \tag{4}$$

with $V_{m,0}(y,z)$ denoting the potential from the m-th atomic layer of the 0-th pillar. In addition, it is satisfied that $V_0(y,z) = \sum_{m=1}^{M} V_{m,0}(y,z)$.

Following the method in BS model,[26] one can obtain

$$V_{m,0}(y,z) = 2\pi\varepsilon_{\mathrm{fs}}\rho_{\mathrm{s}}\sigma_{\mathrm{fs}}^2\left[\Psi_{12}\left(y_{m,0}^{+},z_m\right) - \Psi_{12}\left(y_{m,0}^{-},z_m\right) - \Psi_{6}\left(y_{m,0}^{+},z_m\right) + \Psi_{6}\left(y_{m,0}^{-},z_m\right)\right] \tag{5}$$

with ρ_{s} being areal density of solid atom in the pillar, and

$$\Psi_6(y,z) = \frac{y}{\sqrt{y^2+z_m^2}}\left[\frac{1}{2}\frac{\sigma_{\mathrm{fs}}^4}{z_m^4} + \frac{1}{4}\frac{\sigma_{\mathrm{fs}}^4}{z_m^2\,(y^2+z_m^2)}\right], \tag{6}$$

$$\Psi_{12}(y,z) = \frac{y}{\sqrt{y^2+z_m^2}}\left[\frac{1}{5}\frac{\sigma_{\mathrm{fs}}^{10}}{z_m^{10}} + \frac{1}{10}\frac{\sigma_{\mathrm{fs}}^{10}}{z_m^8\,(y^2+z_m^2)} + \frac{3}{40}\frac{\sigma_{\mathrm{fs}}^{10}}{z_m^6\,(y^2+z_m^2)^2} + \frac{1}{16}\frac{\sigma_{\mathrm{fs}}^{10}}{z_m^4\,(y^2+z_m^2)^3} + \frac{7}{128}\frac{\sigma_{\mathrm{fs}}^{10}}{z_m^2\,(y^2+z_m^2)^4}\right]. \tag{7}$$

In Eq. (5), the relative coordinates $y_{m,0}^{\pm} = \pm w_1/2 - y$, $z_m = z_{s,m} - z$ have been defined. $z_{s,m}$ stands for the z coordinate of the m-th atom layer in the pillars. Details about the derivation of $V_{m,0}(y,z)$ can be found in the supporting information.

For the rectangular corrugated slit pore, the total potential felt by the test fluid atom can be expressed as the sum of potential from each substrate, that is,

$$V_{\mathrm{tot}}(y,z) = V_{\mathrm{subs}}(y,z) + V_{\mathrm{subs}}(y,H-z), \tag{8}$$

where H is the separation of basal walls on the two opposite substrates, as shown in Fig. 1(a). Performing FEA calculation, one can map the 2D solid–fluid potential to an effective 1D potential, which is only z-dependent, that is,

$$\beta V_{\mathrm{eff}}(z) = -\ln\left\{\frac{1}{L_y(z)}\int \exp\left[-\beta V_{\mathrm{tot}}(y,z)\right]\mathrm{d}y\right\}. \tag{9}$$

Here, $\beta = 1/k_{\mathrm{B}}T$ with k_{B} and T being the Boltzmann constant and absolute temperature, respectively. In Eq. (9), $L_y(z)$ is the accessible length in y-direction for the fluid atom at a height of z. The details for derivation of Eq. (9) can also be found in the supporting information. Due to the mean field treatment in the calculation of $V_{\mathrm{eff}}(z)$, the potential in Eq. (9) is referred as a MF-AW-FEA model.

In general cases, the pillars on the opposite substrates may be out of phase with each other. This may exert an effect on the 2D potential, and then on the effective potential $V_{\mathrm{eff}}(z)$. For simplicity, the present work considers only the case in which pillars on opposite substrates are symmetrical with respect to the plane $z = H/2$.

3. Density functional theory for inhomogeneous fluids

According to statistical mechanics, the equilibrium density in inhomogeneous fluids can be determined by minimizing the grand potential functional $\Omega[\rho]$. For the slit pore system under consideration, it can be expressed as[52]

$$\Omega[\rho(z)] = F[\rho(z)] + \int \rho(z)\left[V_{\mathrm{ext}}(z) - \mu\right]\mathrm{d}z. \tag{10}$$

Here, $F[\rho]$ is the Helmholtz free energy functional, while $V_{\mathrm{ext}}(z)$ is the external potential, which should be replaced with $V_{\mathrm{eff}}(z)$ in the MF-AW-FEA model. In addition, μ denotes the chemical potential in the bulk phase.

According to the Barker–Henderson scheme,[53] one can split the fluid–fluid interaction into repulsive and attractive parts, that is,

$$\varphi_{\rm ff}(r)=\begin{cases}\infty, & r<d,\\ 0, & d<r\leq\sigma,\\ \varphi_{\rm ff,att}(r), & \sigma<r\leq r_{\rm c},\\ 0, & r>r_{\rm c},\end{cases} \tag{11}$$

with $r_{\rm c}$ and d being cut-off of LJ potential and effective hard sphere diameter, respectively. In addition, $\varphi_{\rm ff,att}(r)$ is defined as

$$\varphi_{\rm ff,att}(r)=\begin{cases}0, & r\leq\sigma,\\ 4\varepsilon\left[\left(\frac{\sigma}{r}\right)^{12}-\left(\frac{\sigma}{r}\right)^{6}\right], & \sigma<r\leq r_{\rm c},\\ 0, & r>r_{\rm c}.\end{cases} \tag{12}$$

In Eq. (11), the effective hard sphere diameter can be accurately reproduced by[54]

$$d=\frac{1+0.2977\,(\beta\varepsilon)^{-1}}{1+0.33163\,(\beta\varepsilon)^{-1}+0.0010477\,(\beta\varepsilon)^{-2}}\sigma. \tag{13}$$

In DFT for simple fluids, the Helmholtz free energy functional is usually decomposed into ideal and excess parts, that is, $F=F_{\rm id}+F_{\rm ex}$. The former can be exactly expressed as

$$\beta F_{\rm id}[\rho(z)]=\int\rho(z)\left\{\ln\left[\rho(z)\Lambda^{3}\right]-1\right\}{\rm d}z \tag{14}$$

with Λ being the de Broglie wavelength.

In contrast, the exact expression for $F_{\rm ex}[\rho(z)]$ is usually unknown for the realistic systems, and some approximation should be made for the implementation of DFT calculations. According to the perturbative split of $\varphi_{\rm ff}(r)$ in Eq. (11), $F_{\rm ex}[\rho(z)]$ can be split into contributions from hard sphere and attractive tail, that is,

$$F_{\rm ex}[\rho(z)]=F_{\rm hs}[\rho(z)]+F_{\rm att}[\rho(z)]. \tag{15}$$

The hard sphere contribution $F_{\rm hs}[\rho(z)]$ is treated by modified fundamental measure theory (MFMT) developed by Yu *et al.*[55]

$$\beta F_{\rm hs}[\rho(z)]=\int\Phi[n_\alpha]\,{\rm d}z. \tag{16}$$

Here, $\Phi[n_\alpha]$ and n_α are reduced free energy density and weighted density, respectively. Specific expressions for $\Phi[n_\alpha]$ and numerical details about n_α can be found in the literature.[55–57]

Furthermore, the weighted density approximation (WDA)[58–61] has been proven to be powerful to treat the long-ranged attractive tail. In WDA, $F_{\rm att}[\rho(z)]$ can be constructed from bulk equation of state (EoS) by replacing the bulk density with a weighted density $\bar{\rho}(z)$ as

$$\beta F_{\rm att}[\rho(z)]=\int\bar{\rho}(z)\,f_{\rm att}(\bar{\rho}(z))\,{\rm d}z \tag{17}$$

with $f_{\rm att}(\rho)$ denoting the attractive contribution of the Helmholtz free energy per particle in bulk phase. $f_{\rm att}(\rho)$ can be obtained by combining the modified Benedict–Webb–Rubin (MBWR)[62] EoS for the LJ fluid and the Carnahan–Starling (CS)[63] EoS for the hard sphere fluid. More details about the WDA calculation can be found in our previous works.[64,65]

Once $F_{\rm ex}[\rho(z)]$ is constructed, the equilibrium density can be calculated by minimizing the grand potential $\Omega[\rho(z)]$, which leads to the Euler–Lagrange equation

$$\ln\rho(z)=\beta\left[\mu-\frac{\delta F_{\rm ex}[\rho(z)]}{\delta\rho(z)}-V_{\rm ext}(z)\right]. \tag{18}$$

Prior to the calculation of $\rho(z)$, $V_{\rm ext}(z)$ should be calculated firstly by Eq. (9). Actually, determination of $V_{\rm ext}(z)$ is straightforward because analytical expression for the 2D fluid–solid potential has been obtained in Eqs. (4)–(8). For an obtained $V_{\rm ext}(z)$, the nonlinear equation, say Eq. (18), is solved in a standard manner by Picard iteration method with the grid size of 0.02σ. The iterations are continued until the sum over the grid points of the absolute values of the differences between two consecutive iterations is smaller than 10^{-6}. In the calculation, the involved numerical integrations and convolutions are all determined by the standard trapezoidal quadrature. More detail about the algorithm of DFT calculation can refer to Ref. [56] and the references in it.

Unlike the case of smooth pore, the involved spatial integration $\iint{\rm d}x{\rm d}y$ in calculations for rough pores is no longer a constant. Instead, it should be z-dependent because the pillars prohibit the fluid particles from entering the region they have occupied, as sketched in Fig. 1(b). Therefore, any volume integral of the form $\iint(\cdot){\rm d}x{\rm d}y{\rm d}z$ should be replaced by $\int(\cdot)A_{\rm acc}(z)\,{\rm d}z$. Here, the z-dependent accessible area $A_{\rm acc}(z)$ can be obtained as follows:

$$\frac{A_{\rm acc}(z)}{A}=\begin{cases}1-\frac{w_1+2\sigma_{\rm fs}}{\lambda}, & z<D,\\ 1-\frac{w_1+2\sqrt{\sigma_{\rm fs}^2-(z-D)^2}}{\lambda}, & D+\sigma_{\rm fs}\geq z\geq D,\\ 1, & z>D+\sigma_{\rm fs},\end{cases} \tag{19}$$

with A the projected area of the whole substrate on its basal wall. For instance, the excess adsorption in the rectangular corrugated slit pore should be calculated as

$$\Gamma_{\rm ex}=\frac{1}{A}\int{\rm d}zA_{\rm acc}(z)\left[\rho(z)-\rho_{\rm b}\right] \tag{20}$$

with $\rho_{\rm b}$ the fluid density in the bulk phase.

4. Results and discussion

In DFT calculations for inhomogeneous fluid, the external potential $V_{\rm ext}(z)$ plays a decisive role because it makes the confined fluid different from the corresponding bulk phase. To understand the potential arising from the rectangular corrugated slit pore, we have calculated the 2D wall potential $V_{\rm tot}(y,z)$.

A contour of $V_{\rm tot}(y,z)$ for argon atom between two adjacent pillars with $w_1/\sigma = w_2/\sigma = D/\sigma = 3.0$ has been presented in Fig. 2. It is obvious that for the given geometry of substrate, the potential $V_{\rm tot}(y,z)$ has a specific distribution near the substrate. It is quite different from that of the smooth pore, because the pillars on the substrate make the potential inhomogeneous along y-direction.

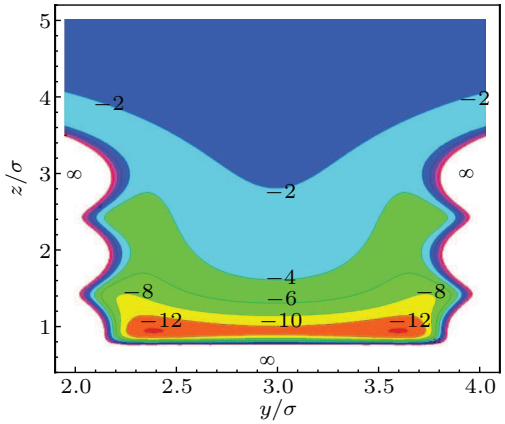


Fig. 2. Contour of the 2D wall potential $\beta V_{\rm tot}(y,z)$ of argon atom between two adjacent pillars. The reduced parameters are set as $w_1/\sigma = w_2/\sigma = D/\sigma = 3.0$, $\sigma_{\rm ss}/\sigma = 1.0$, $\varepsilon_{\rm ss}/\varepsilon = 1.0$ and $\rho_{\rm s}\sigma^3 = 1.0$.

In order to apply the MF-AW-FEA model to the DFT calculations, we have calculated the 1D effective solid–fluid potential in the rectangular corrugated slit pores with different geometry. The results for argon at 87.3 K are shown in Figs. 3(a)–3(c). For the purpose of comparison with the results from RC-AW-FEA model,[50] which has simulated the potential from one single rough wall, the pore width in our calculation has been set as $H/\sigma = 20.0$. This pore width is large enough to regard that the two corrugated substrates are immune to each other. In addition, other parameters in the MF-AW-FEA calculations are set the same as those used in the simulation, which has been listed in Table 1.

Table 1. Parameters used for calculation of $V_{\rm ext}(z)$ with the MF-AW-FEA model; in Figs. 3 and 4(c) for argon at 87.3 K, while in Figs. 7 for CO_2 at 273 K.

Species	$\sigma_{\rm ff}$ (nm)	$\varepsilon_{\rm ff}/k_{\rm B}$ (K)	$\sigma_{\rm sf}$ (nm)	$\varepsilon_{\rm sf}/k_{\rm B}$ (K)	p_0 (bar)
Ar	0.3405	119.8	0.34025	57.92	1.0
CO_2	0.349	227.9	0.344	79.9	34.7

Figure 3(a) presents the 1D effective external potential near a rectangular corrugated substrate with $w_1/\sigma = w_2/\sigma = 3.0$ and $D/\sigma = 1.0$–4.0. Obviously, the potential from MF-AW-FEA shows a similar pattern to that of potential from RC-AW-FEA.[50] Specifically, each curve has two minima, one at $z_1 \approx \sigma$, while the other at $z_2 \approx D+\sigma$. Actually, the minimum at z_2 arises from the attraction of top surface of the pillars. In the case of $D/\sigma = 1$, the result from MF-AW-FEA is slightly higher than that from RC-AW-FEA. This stems from the different manner in which the roughness of substrate is modeled. That is, the substrate is defined to be rectangular corrugated in the MF-AW-FEA model, while it is random sampled in RC-AW-FEA model. Furthermore, it is shown that for a larger D, the potential curve is generally lowered in between the two minima. This can be attributed to the enlarged lateral area generated by higher pillars, which provide more adsorptive sites on the microscopic point of view.

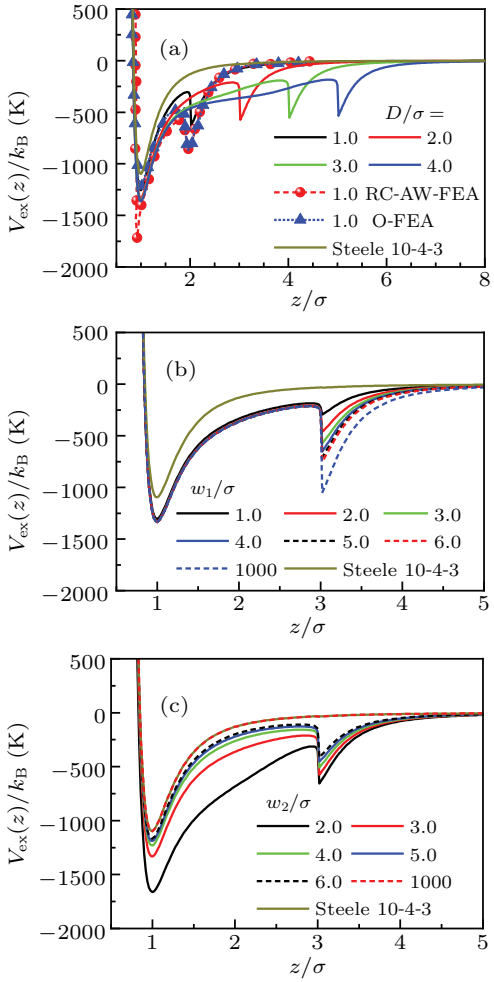


Fig. 3. MF-AW-FEA model of the potential for argon atom in the rectangular corrugated pores of different parameters, but all with $H/\sigma = 20$. (a) Effect of D on $V_{\rm ext}(z)$. Lines are results from MF-AW-FEA with $w_1/\sigma = w_2/\sigma = 3.0$, while lines with symbol are those from RC-AW-FEA and O-FEA by MC simulation.[50] (b) Effect of w_1 on $V_{\rm ext}(z)$, with $w_2/\sigma = 3.0$ and $D/\sigma = 2.0$. (c) Effect of w_2 on $V_{\rm ext}(z)$, with $w_1/\sigma = 3.0$ and $D/\sigma = 2.0$.

Effect of w_1 on the 1D effective external potential is depicted in Fig. 3(b). Obviously, the two minima on each curve coincide at the same position because the height of the pillars has been fixed. Further comparison suggests that the potential is lowered with the increase of w_1, especially in the region near the top of the pillars. Actually, larger w_1 corresponds to wider top area of the pillars. By averaging along y-direction, this leads to stronger attraction there. Further, the effect of w_2 on the 1D effective external potential is presented in Fig. 3(c). It is obvious that the effect of w_2 on the potential is just opposite to that of w_1. For the case of $w_2/\sigma = 1000$, the potential curve coincides completely with that of Steele 10–4–3 poten-

tial, which indicates the vanishing influence of the pillars in this limiting case.

Having obtained the effective 1D potential for the rectangular corrugated pores, one can proceed with calculations for the structure and thermodynamic properties of fluid in these pores. However, it is necessary to check the performance of our DFT calculation at first. To this end, we perform calculation for confined LJ fluid in a smooth slit pore, which is modelled by Steele 10–4–3 potential. The results in Fig. 4(a) suggest a good agreement between DFT results and those from MC simulations.[66]

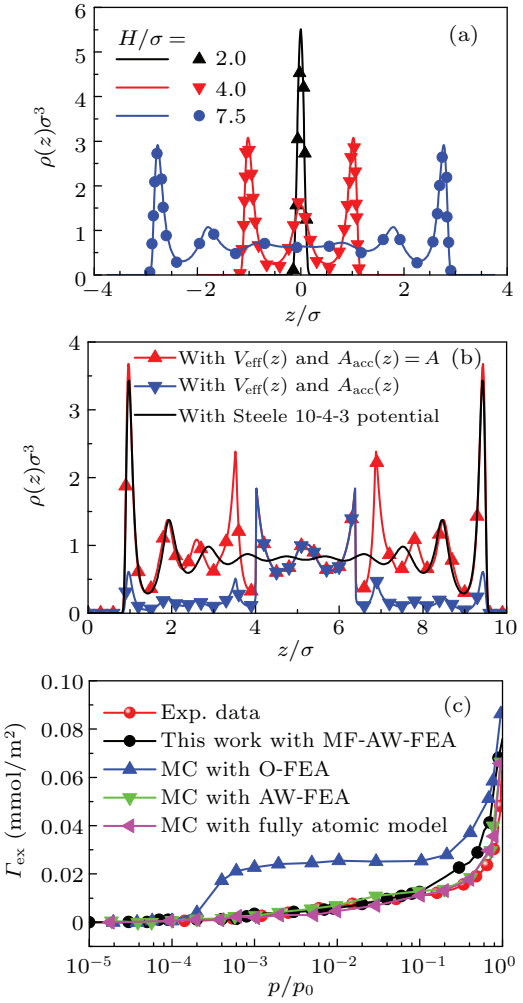


Fig. 4. (a) Density profiles of LJ fluid confined in smooth slit pores with $k_{\rm B}T/\varepsilon = 1.2$ and $\rho_{\rm b}\sigma^3 = 0.5925$. Lines are results from our DFT calculations, while symbols are results from MC simulations.[66] (b) Density profile of argon fluid confined in a smooth pore and rectangular corrugated pore with $w_1/\sigma = w_2/\sigma = D/\sigma = 3.0$. In both calculations, we set $\rho_{\rm b}\sigma^3 = 0.8$, $k_{\rm B}T/\varepsilon = 1.2$ and $H/\sigma = 10.4$. (c) Excess adsorption isotherms of argon at 87.3 K on the BP-280 solid by different models of pore potential. For the purpose of comparison, experimental data[67] and GCMC results[50] are also included.

Example sets of density profile for fluid in rectangular corrugated slit pores are shown in Fig. 4(b). In the calculation, parameters are set as $w_1/\sigma = w_2/\sigma = D/\sigma = 3.0$, $H/\sigma = 10.4$, $k_{\rm B}T/\varepsilon = 1.2$, and $\rho_{\rm b}\sigma^3 = 0.8$. As stated above, fluid particles cannot enter the region that the pillars have occupied. Therefore, the accessible region should be considered, and the density output by the DFT calculation should multiply the quality $A_{\rm acc}(z)/A$. As shown in Fig. 4(b), both density curves, with and without the consideration of $A_{\rm acc}(z)$, show maximum at $z = 4\sigma$, which implies the minimum of $V_{\rm eff}(z)$ there. In contrast, both curves coincide between 4σ and 6.4σ because $A_{\rm acc}(z)/A = 1$ in this region. Furthermore, comparison of $\rho(z)$ between smooth and corrugated pores shows that they are markedly different, especially in the region near the top surface of the pillars. This indicates that the pillars can significantly modulate the fluid structure in the corrugated pore.

In order for a further verification of the efficiency of the MF-AW-FEA model, calculation for the excess adsorption isotherms of argon on BP-280 solid is performed at $T = 87.3$ K. The result with $w_1/\sigma = 7$, $w_2/\sigma = 3.0$ and $D/\sigma = 1.0$ is given in Fig. 4(c). In the figure, results from experimental measurement[67] and GCMC simulation[50] are also presented for a purpose of comparison. In the calculation, the pore width is set as $H/\sigma = 20.0$. Evidently, the DFT result agrees very well with the experimental data in the region $p/p_0 \in (10^{-5}, 0.1)$. With a further increase of p, the curve shows a modest deviation from the data. The deviation can be ascribed to the mean-field treatment in the MF-AW-FEA model. Even so, the DFT result with MF-AW-FEA model still shows better agreement with experimental data than GCMC results with O-FEA model, in the region of $p/p_0 \in (10^{-4}, 1)$.

4.1. Excess adsorption isotherms

Excess adsorption is important in either theoretical or engineering analysis, and may provide noteworthy information about the global behavior of confined fluids. To understand the effect of pore geometry on excess adsorption $\Gamma_{\rm ex}$, adsorption isotherms of confined LJ fluids in the rectangular corrugated slit pores are calculated in different cases of H, D, w_1, and w_2. The results are given in Figs. 5 and 6. In Fig. 5, dependence of $\Gamma_{\rm ex}$ on H for LJ fluid confined in smooth slit pores is firstly calculated with $k_{\rm B}T/\varepsilon = 1.2$ and $\rho_{\rm b}\sigma^3 = 0.5925$. Comparison with MC results[68] shows that they agree well.

In Figs. 5, results for excess adsorption with $w_1/\sigma = 1$–6 show that for each value of w_1, $\Gamma_{\rm ex}$ presents oscillatory increase with H. This can be understood as follows. For the pore width that gives a maximum of $\Gamma_{\rm ex}$, the fluid configuration in the pore is more ordered, which indicates that the particles are efficiently arranged in layer structures, and the available space is utilized in a better way. In addition, the period of oscillation is nearly one diameter, which displays the influence of hard sphere excluded volume on determining the packing of the confined fluid. Further comparison between the curves shows that the oscillation of $\Gamma_{\rm ex}$ and its amplitude are enhanced by larger w_1, which indicates the constructive influence of w_1 on $\Gamma_{\rm ex}$.

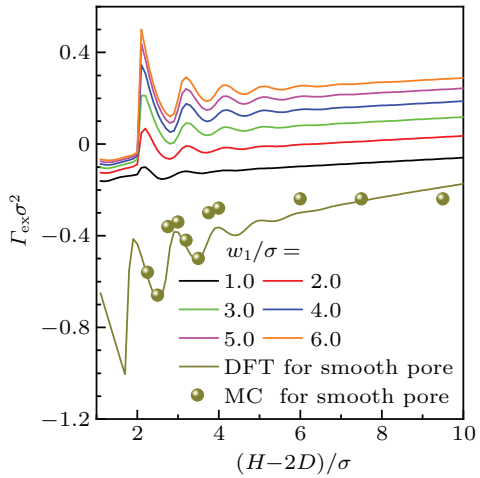


Fig. 5. Dependence of Γ_{ex} on H for confined LJ fluids in the rectangular corrugated pores with different w_1. Other parameters are set as $k_BT/\varepsilon = 1.2$, $\rho_b\sigma^3 = 0.5925$, $w_2/\sigma = 3.0$ and $D/\sigma = 2.0$. In calculation for smooth pore, we set $k_BT/\varepsilon = 1.2$ and $\rho_b\sigma^3 = 0.5925$, which are the same as those used in MC simulations.[68]

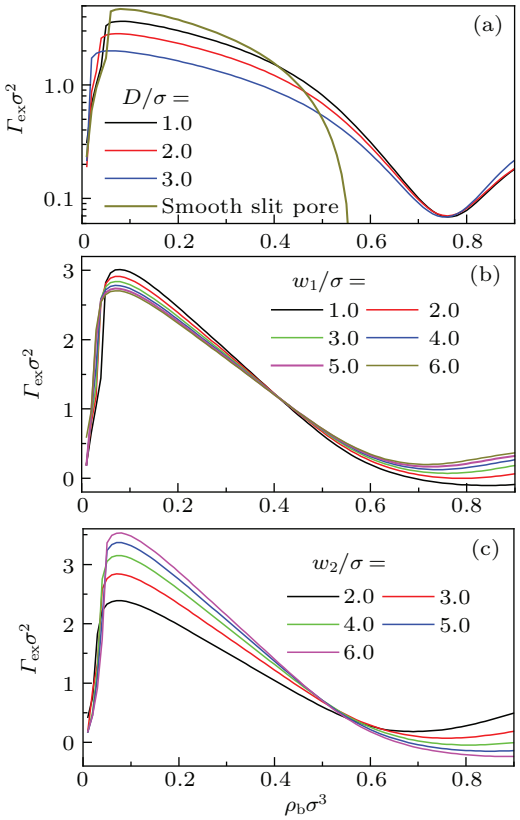


Fig. 6. Excess adsorption isotherms of confined LJ fluids in different rectangular corrugated slit pores. $k_BT/\varepsilon = 1.2$ and $H/\sigma = 10.0$ has been set in the calculations. Specifically, (a) dependence of isotherms on D with $w_1/\sigma = w_2/\sigma = 3.0$. (b) dependence of isotherms on w_1 with $w_2/\sigma = 3.0$ and $D/\sigma = 2.0$. (c) dependence of isotherms on w_2 with $w_1/\sigma = 3.0$ and $D/\sigma = 2.0$. In (a), logarithmic axis is used to show its variation in the high density region.

It is evident in Fig. 6(a) that in the low and high density regions, the height of pillar exerts an opposite influence on Γ_{ex}. Actually, there is a competitive mechanism about the effect of D on Γ_{ex}. For a larger D, the higher pillar leads to an adsorptive effect because it provides more adsorptive sites. On the other hand, larger D leads to wider depletion layer around the pillar. This depletion region prohibits the particle from entering, and then depresses the adsorption. The winner in the competition depends on the density in the pore. For sufficiently large densities, multi-layer structures occur in the pore, and then the former is dominant. In contrast, for low densities, the latter holds an advantage, because the increase of Γ_{ex} arising from additional adsorptive sites is not enough to compensate the decrease of Γ_{ex} arising from the enlargement of the depletion layer.

Results in Fig. 6(b) suggest that w_1 has the same effect on Γ_{ex} as D. With the increase of w_1, the adsorptive effect and depletion effect win their competition in high density and low density region, respectively. However, the switching point has been shifted leftwards. This implies that the advantage of depletion effect has been depressed in its competition with the adsorptive effect, because the depletion layer keeps unchanged as w_1 varies. In contrast, Fig. 6(c) shows that the effect of w_2 on Γ_{ex} is opposite to that of w_1. With the increase of w_2, the adsorptive effect of the pillars is weakened, because its attraction has been lowered by the area-weighted average in a larger spatial region.

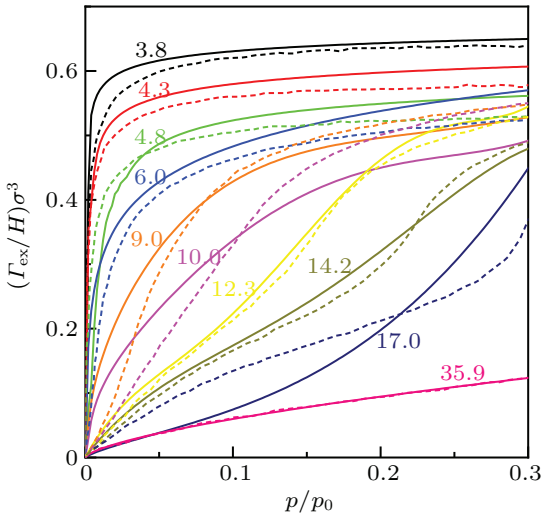


Fig. 7. Excess density of CO_2 confined in sinusoidal corrugated slit pore with different widths. The solid and dashed lines are results of this work and 2D-NLDFT[69] calculation, respectively. Note that lines with the same color correspond to results for the identical pore width. The number in the figure denote the pore width, but in units of Å.

It is necessary to point out that the procedure proposed here should not be limited to this specific roughness, but should be applicable for other complex, or even random surface, so long as its shape or geometry can be mathematically described. As a test, we perform calculations for confined CO_2 in a sinusoidal corrugated slit pore, which has been investigated with 2D-NLDFT by Jagiello *et al.*[69] Based on the 2D wall potential proposed by Jagiello *et al.*, an effective 1D wall potential can be calculated by using the MF-AW-FEA model. The parameters in the calculation has been given in Table 1. The excess densities of confined CO_2 at 273 K

are shown in Fig. 7. The comparison with results from 2D-NLDFT suggests that they agree well for all the chosen pore widths. This demonstrates the good performance of the MF-AW-FEA model in its application to other rough pores.

4.2. Solvation force

In smooth slit pore, solvation force is the normal force exerted by the fluid on per unit area of each wall. Its oscillating behavior has been confirmed in smooth pores. However, solvation force between some non-crystalline surfaces may be different due to their molecularly roughness on the surfaces. To understand the effect of roughness on solvation force, calculations are performed for the LJ fluid confined in the rectangular corrugated slit pore. In the context of thermodynamics, the solvation force can be expressed as[70]

$$f_{\rm s} = -\frac{1}{A}\left(\frac{\partial \Omega_{\rm ex}}{\partial H}\right)_{\mu,T}. \tag{21}$$

Here, excess grand potential $\Omega_{\rm ex} = \Omega + pV$ with p the bulk pressure, and A refers to the projected area of the substrates. Note that the effect of pillars on $f_{\rm s}$ has been taken into account in the calculation of $\Omega_{\rm ex}$.

Firstly, the dependence of $f_{\rm s}$ on H is calculated for the confined LJ fluid in rectangular corrugated slit pores. The results in Fig. 8 show that for each case of D, $f_{\rm s}$ exhibits oscillating behavior with H. Moreover, the period of oscillation is nearly one diameter of the fluid particle. For the same reason as that for the oscillation of $\Gamma_{\rm ex}$ in Fig. 5, the oscillation of $f_{\rm s}$ stems from the variation of the ordered configuration of fluids in the pore. Obviously, each curve exhibits a maximum near $(H-2D)/\sigma = 2.0$. This maximum corresponds to an ordered layer structure in the fluid, while the subsequent maxima in the curve indicate the newly formed layers in the pore. In addition, the solvation force is generally negative for the pore satisfies $(H-2D)/\sigma < 2.0$, which indicates an attraction between the opposite walls.

It is apparent in Fig. 8 that the oscillation amplitude of $f_{\rm s}$ for the rectangular corrugated pore is much smaller than that for the smooth slit pore. Moreover, the oscillation amplitude of $f_{\rm s}$ is weakened as D is increased. As D is large enough, its influence on $f_{\rm s}$ may be too small to be distinguished. This can be ascribed to the higher pillars, which destroy the ordered layer structure, and then weaken the normal pressure and solvation force in the pore. Actually, in order to quantify the effect of geometrical roughness on solvation force, Frink *et al.*[71] had proposed an empirical fitting with an exponentially decaying oscillatory function. According to their fitting, the oscillation amplitude of the solvation force decreases significantly with the roughness, though a weak increase occurs as the roughness is further increased. Obviously, this is consistent with the results in Fig. 8.

In order for a better understanding of the effect of roughness on $f_{\rm s}$, the dependences of $f_{\rm s}$ on w_1 and w_2 are also calculated. The results are given in Fig. 9. Results in Fig. 9(a) show that for the given value of H and other chosen parameters, $f_{\rm s}$ increases monotonously with w_1, while its rate of increase decreases with H. When H is large enough, $f_{\rm s}$ may become independent on w_1, just as shown in the case of $H/\sigma = 12.0$. While in Fig. 9(b), w_2 shows an opposite effect on $f_{\rm s}$. This can be understood by the superposition approximation,[71,72] which interprets the solvation force in rough pore as a weighted average of those in several smooth pores of different width. For the rectangular corrugated slit pore under consideration, it involves only two types of smooth slit pore of widths H and $H-D$. For the given H and D, increasing of w_1 leads to a larger weight of the smooth pore of width $H-D$. This causes an enhancement of $f_{\rm s}$, because $f_{\rm s}$ in narrower pores is stronger than that in wider pores. On the contrary, increasing of w_2 corresponds to a larger weight of the wider smooth pore of width H, which interprets the reason why $f_{\rm s}$ decreases with w_2, as shown in Fig. 9(b).

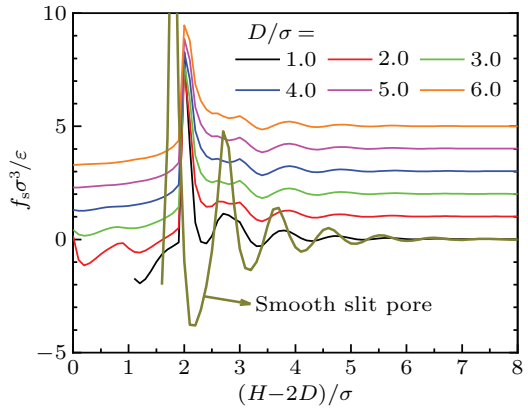


Fig. 8. Dependence of $f_{\rm s}$ on H under different conditions of D. $w_1/\sigma = w_2/\sigma = 3.0$, $\rho_{\rm b}\sigma^3 = 0.8$ and $k_{\rm B}T/\varepsilon = 1.2$ are set in the calculations. For the purpose of comparison, the corresponding results for smooth pore is given by the dark yellow line. Note that except the curve for $D/\sigma = 1.0$, other curves have been shifted up by 1 in turn from bottom to top.

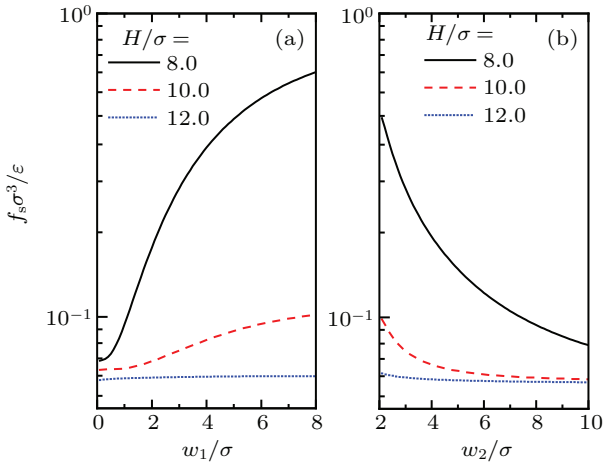


Fig. 9. Effects of w_1 and w_2 on $f_{\rm s}$ for confined LJ fluids with $\rho_{\rm b}\sigma^3 = 0.8$, $k_{\rm B}T/\varepsilon = 1.2$ and $D/\sigma = 2.0$. For (a), $w_2/\sigma = 3.0$, while for (b), $w_1/\sigma = 3.0$.

4.3. Absolute and relative surface free energies

For fluid near smooth substrate or in pores, surface tension can be well defined in formal thermodynamics. However, surface tension in rough pores gets more complicated because the complex geometry may result in inhomogeneity and anisotropy of the surface tension.[73] Besides, the rough geometry and the anisotropy of surface tension make it a difficult task to determine the surface of "tension", because it depends heavily on the geometrical characteristics of the rough substrate. In contrast, calculation of surface free energy is more convenient, since it is a global measurement of the whole system.

According to the formal statistical mechanics, surface free energy in a slit pore can be calculated as the excess grand potential per unit area over that of bulk phase[74]

$$\omega_{\rm s} = \frac{\Omega\left[\rho\left(z,H\right)\right] - \Omega_{\rm b}}{2A} \tag{22}$$

with $\rho\left(z,H\right)$ standing for the density in a pore of width H.

Besides, Frink *et al*. have also defined a relative surface free energy on unit area as[71]

$$\Delta\omega_{\rm s} \equiv \frac{\Omega_{\rm ex}\left(H\right) - \Omega_{\rm ex}\left(\infty\right)}{2A}, \tag{23}$$

where $\Omega_{\rm ex}\left(H\right)$ stands for the excess grand potential in the pore of a width H, while $\Omega_{\rm ex}\left(\infty\right)$ represents that in the limit case of $H\to\infty$. Physically, Eq. (22) defines an absolute surface free energy, while $\Delta\omega_{\rm s}$ in Eq. (23) is a relative measurement of the surface energy for fluid in pore with finite H over that in a reference pore. Therefore, the minimum of $\Delta\omega_{\rm s}$ may supply information about the equilibrium separation the two substrates.

In order to obtain useful insight to understand interfacial phenomena near rough substrates, both $\omega_{\rm s}$ and $\Delta\omega_{\rm s}$ for LJ fluids confined in a rectangular corrugated slit pore have been calculated with $\rho_{\rm b}\sigma^3 = 0.8$ and $k_{\rm B}T/\varepsilon = 1.2$. Effects of H, w_1 and w_2 are given in Fig. 10. In Figs. 10(a) and 10(d), comparison between results of $\omega_{\rm s}$ and $\Delta\omega_{\rm s}$ in different cases of D suggests that $\omega_{\rm s}$, $\Delta\omega_{\rm s}$, and their oscillating amplitudes with H are all depressed with the increasing D. The pillars on the substrate should be responsible for the depression because higher pillars may destroy the ordered layer structure of fluid in the pore.

Further, Fig. 10(a) shows that for each value of H, $\omega_{\rm s}$ becomes more negative as D increases. In the Young's scheme, it corresponds to smaller contact angle and enhanced hydrophilicity of the wall.[75] This results from the expanded lateral surface and more adsorptive sites on it. Further, as H is increased, each $\omega_{\rm s}$ curve decreases to an asymptotic value, which corresponds to the isolated substrate case. In Fig. 10(b), $\omega_{\rm s}$ decreases monotonously with w_1 for each value of H. This can be ascribed to the enhanced confinement effect that arising from the narrow space between the top surface of pillars on the opposite substrates. For the obvious reason, effect of w_2 on $\omega_{\rm s}$ is just opposite to that of w_1, as shown in Fig. 10(c).

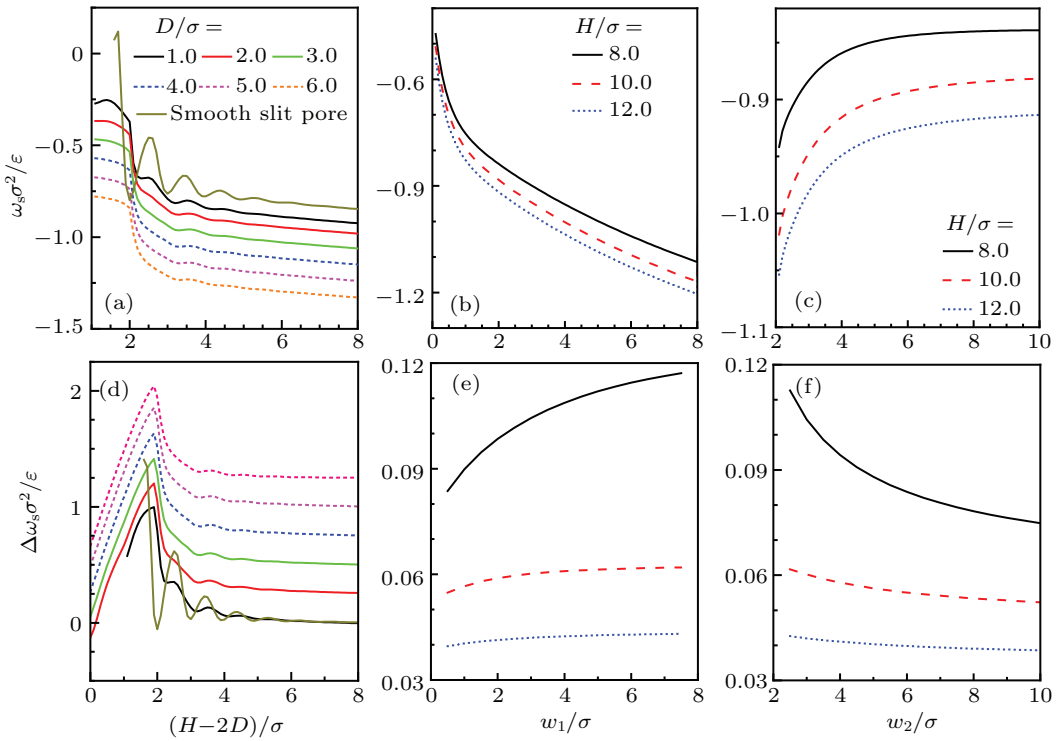


Fig. 10. The $\omega_{\rm s}$ and $\Delta\omega_{\rm s}$ of confined LJ fluids with $\rho_{\rm b}\sigma^3 = 0.8$ and $k_{\rm B}T/\varepsilon = 1.2$. (a)–(c) Dependence of $\omega_{\rm s}$ on H, w_1 and w_2 under different conditions. (d)–(f) Dependence of $\Delta\omega_{\rm s}$ on H, w_1 and w_2 under different conditions. Specifically, in (a) and (d), $w_1/\sigma = w_2/\sigma = 3.0$. In (b) and (e), $w_2/\sigma = 3.0$, $D/\sigma = 2.0$. In (c) and (f), $w_1/\sigma = 3.0$, $D/\sigma = 2.0$. The curves in (d) have been shifted up by 0.25 in turn from bottom to top, except that for $D/\sigma = 1.0$.

Results for $\Delta\omega_s$ are given in Figs. 10(d)–10(f). Obviously, $\Delta\omega_s$ exhibits extremely weak dependence on D, and it tends to zero when H is sufficiently large. As also shown in Figs. 10(e) and 10(f), w_1 and w_2 modulate $\Delta\omega_s$ in an opposite manner, while they exert an extremely weak influence on $\Delta\omega_s$ as H is large enough. Unlike ω_s in Fig. 10(b), $\Delta\omega_s$ in Fig. 10(e) monotonously increases with w_1 for each case of H. This means that wider pillars enhance the correlation between the opposite corrugated substrates, and then leads to larger $\Delta\omega_s$, as suggested by the superposition approximation.[71]

4.4. Thermodynamic response functions

Thermodynamic response functions, which are defined as the first derivative of fundamental thermodynamics qualities, provide rich information about critical behavior and phase transition. However, there are too many such derivatives and relations between them. Actually, Bridgman[76] had picked out three fundamental members, and all other response functions can be expressed in terms of the three. These three functions are isobaric thermal expansivity α_P, isothermal compressibility κ_T and isobaric heat capacity C_P (in NPT ensemble). Note that for canonical ensemble, C_P should be replaced by isochoric heat capacity C_V, which relates C_P via the relation $C_P = C_V + TV\alpha_P^2\kappa_T^{-1}$.[77] Here, V is the volume of the fluid.

By utilizing the fundamental thermodynamic relation, the above thermodynamic response functions are usually calculated as[77]

$$\begin{aligned}
\alpha_P &\equiv \left(\frac{\partial V}{\partial T}\right)_P = -\frac{1}{\rho}\left(\frac{\partial \rho}{\partial T}\right)_P, \\
\kappa_T &\equiv -\frac{1}{V}\left(\frac{\partial V}{\partial p}\right)_T = \frac{1}{\rho}\left(\frac{\partial p}{\partial \rho}\right)_T^{-1}, \\
C_V &\equiv \left(\frac{\partial U}{\partial T}\right)_V = -T\left(\frac{\partial^2 F}{\partial T^2}\right)_V.
\end{aligned} \tag{24}$$

Actually, these scalar equations are originally defined for uniform bulk phase. However, in confined fluids, some of these properties may be position-dependent or even tensors. Takes the isothermal compressibility κ_T in confined fluid for example, one should calculate its components by using the corresponding components of pressure tensor. However, in an ultrasonic experiment for κ_T in confined fluid, its anisotropy cannot be measured experimentally. Therefore, one usually regards κ_T as a scalar or an averaged macroscopic value, with which the confined fluid is regarded as a whole. This is likely to represent the experimental observable in ultrasonic experiment. Similarly, in the calculation of the thermodynamic response functions, one can also regard them as averaged macroscopic quantities, though they maybe position-dependent on the atomistic level.

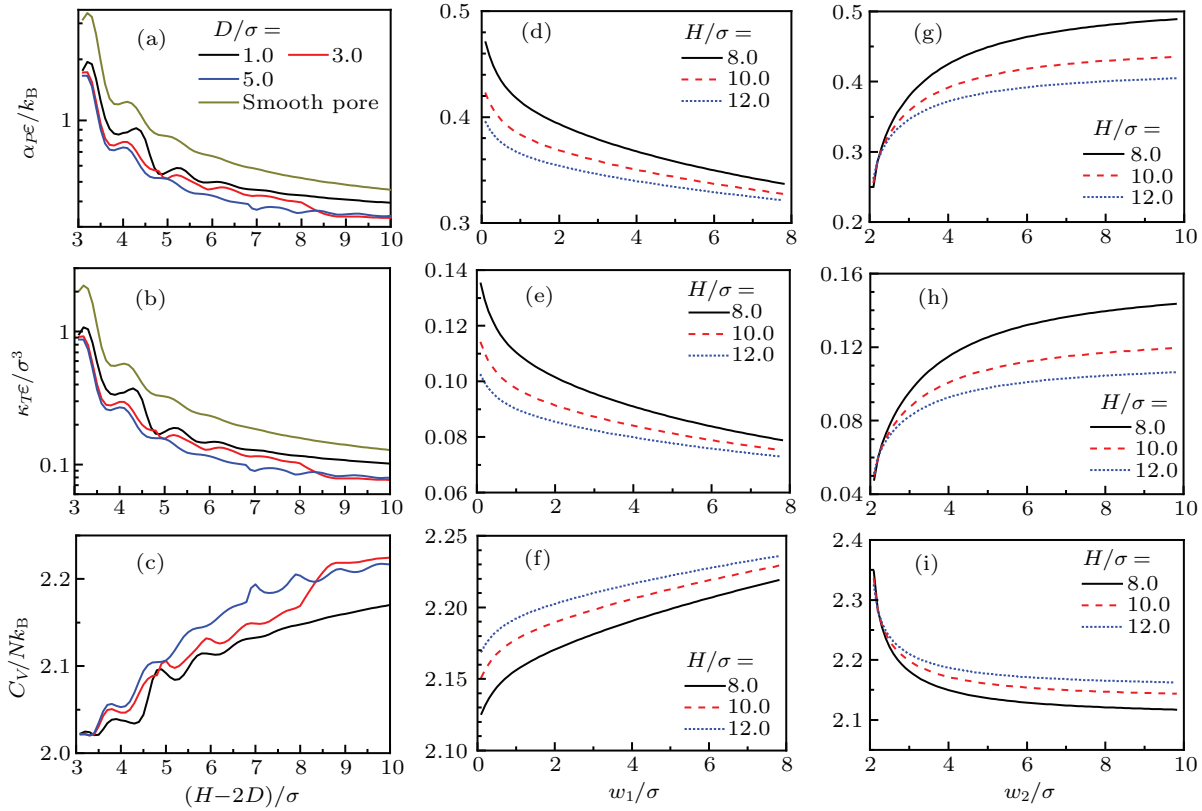


Fig. 11. Dependence of α_P, κ_T and C_V on H, w_1 and w_2 for confined LJ fluids with $\rho_b\sigma^3 = 0.8$ and $k_BT/\varepsilon = 1.2$. The top, middle and bottom rows are results for α_P, κ_T and C_V, respectively. The left, middle and right columns show respectively the H, w_1 and w_2 dependence of thermodynamic response functions. The same type of lines in each column correspond to the same value of parameters in calculations. Specifically, (a)–(c) $w_1/\sigma = w_2/\sigma = 3.0$, (d)–(f) $w_2/\sigma = 3.0$ and $D/\sigma = 2.0$, (g)–(i) $w_1/\sigma = 3.0$ and $D/\sigma = 2.0$.

Relations between state parameters of the fluid are required in the calculation of these response functions. This can be obtained from the existing EoS, such as those proposed by Tang and Lu,[78] Kolafa and Nezbeda,[79] Mecke *et al.*[80] or MBWR[62] for LJ fluids. To keep consistency with the WDA in the DFT calculations, we have employed the MBWR EoS. Furthermore, in order to take into account the effects of confinement and pore roughness, we replace $\rho_{\rm b}$ with an averaged pore density $\rho_{\rm av} \equiv \frac{1}{H}\int_0^H {\rm d}z\rho(z)$, which contains information about confinement and roughness.

Figures 11(a), 11(d) and 11(g) present results for α_P of confined LJ fluids in rectangular corrugated slit pores. Figure 11(a) shows that α_P descends oscillatorily with H. The oscillatory behavior results again from the ordered configuration of the fluid in the pore, while its decline can be understood by the increase of $\rho_{\rm av}$ with H, which has been shown in Fig. 5. In a denser fluid, the stronger excluded volume depresses its expansion with temperature, and then leads to a smaller α_P. In addition, decreasing of α_P with D stems from the enlargement of lateral area around the pillars, which may adsorb more particles and then depresses α_P. Influences of w_1 and w_2 on α_P are given in Figs. 11(d) and 11(g), respectively. As shown in Fig. 6(b), $\rho_{\rm av}$ increases with w_1 for the bulk density $\rho_{\rm b}\sigma^3 = 0.8$. Therefore, as w_1 increases, α_P should be depressed by the enhanced excluded volume in the fluid. The influence of w_2 on α_P is just on the opposite.

Results of κ_T for LJ fluid in rectangular corrugated slit pore are given in Figs. 11(b), 11(e) and 11(h). Obviously, influences of H, D, w_1 and w_2 on κ_T have the same patterns as those on α_P. This is owing to the fact that fluid is more difficult to deform for a larger average density. In contrast, influences of H, D, w_1 and w_2 on C_V of LJ fluid in corrugated slit pore is just opposite to those on α_P and κ_T. This is because in a fluid with larger average density, stronger correlation between particles results in an increase of inter energy, and then its isobaric heat capacity C_V. This is consistent with the results presented in Figs. 11(c), 11(f) and 11(i).

5. Conclusion

In conclusion, structural and thermodynamic properties of confined LJ in rectangular corrugated slit pores are investigated by classical density functional theory. At first, a method for effective 1D solid–fluid potential, say the MF-AW-FEA model, is proposed for the rectangular corrugated slit pore. Application of this effective 1D potential to the adsorption of argon on BP-280 has verified its ability and effectiveness in the investigation of fluids near rough surface. Further, the effective 1D potential has been employed to calculate the structure of LJ fluids confined in rectangular corrugated slit pore of different geometrical characteristics. Based on the obtained density in the corrugated pore, the thermodynamic properties including excess adsorption isotherms, solvation force, surface free energy, and thermodynamic response functions of fluids, are calculated respectively. The influences of pore geometry on these properties are investigated.

The results suggest that the geometrical parameters including H, w_1, w_2 and D of the rectangular corrugated slit pore, have distinct influences on these properties. Firstly, the increase of w_1 or D can enhance these properties, while w_2 shows an opposite effect. Secondly, these properties usually exhibit oscillation with pore width due to the variation of the ordered configuration of fluid in the pore. The amplitude of the oscillation can also be modulated by the geometrical characteristics of the pore. Thirdly, in the limiting case of $w_1 \to \infty$ or $w_2 \to \infty$, the corrugated pore approaches to a smooth pore of specific width, and these thermodynamic properties tend to those of the corresponding smooth pore. In summary, these results provide us some novel and interesting insight about the fluids confined in rough pores. It is expected to be helpful to explore relevant issues including wetting, bubble, droplet and other interfacial phenomena near surfaces of complex topology.

Acknowledgements

Project supported by the National Natural Science Foundation of China (Grant No. 21503077), the Fundamental Research Fund for the Central Universities of China (Grant No. 2020MS147), and the Science and Technology Project of Hebei Education Department, China (Grant No. QN2018119).

References

[1] Zhang S, Wei K, Xiao Y, Ma X H, Zhang Y C, Liu G G, Lei T M, Zheng Y K, Huang S, Wang N, Asif M and Liu X Y 2018 *Chin. Phys. B* **27** 097309
[2] Sun C Z, Zhou R F, Zhao Z X and Bai B F 2020 *J. Phys. Chem. Lett.* **11** 4678
[3] Davis M E 2002 *Nature* **417** 813
[4] Thommes M and Cychosz K A 2014 *Adsorption* **20** 233
[5] Alothman Z A 2012 *Materials* **5** 2874
[6] Liu P S and Chen G F 2014 *Porous Materials: Processing and Applications* (New York: Elsevier)
[7] Yang H Q, Xu Z H, Fan M H, Gupta R, Slimane R B, Bland A E and Wright I 2008 *J. Environ. Sci.* **20** 14
[8] Sanz-Pérez E S, Murdock C R, Didas S A and Jones C W 2016 *Chem. Rev.* **116** 11840
[9] Choi S, Drese J H and Jones C W 2009 *Chem. Sus. Chem.* **2** 796
[10] Wilms D, Winkler A, Virnau P and Binder K 2010 *Phys. Rev. Lett.* **105** 045701
[11] Schneider D, Kondrashova D and Valiullin R 2017 *Sci. Rep.* **7** 7216
[12] Krekelberg W P, Siderius D W, Shen V K, Truskett T M and Errington J R 2013 *Langmuir* **29** 14527
[13] Liu Y, Lorusso D, Holdsworth D W, Poepping T L and de Bruyn J R 2018 *J. Non-Newton Fluid* **261** 25
[14] Shen Z Y, Farutin A, Thiébaud M and Misbah C 2017 *Phys. Rev. Fluids* **2** 103101
[15] Peng B and Yu Y X 2008 *Langmuir* **24** 12431
[16] Sun Z L, Kang Y S, Kang Y M, Liu Z C and Ma H X 2012 *Chin. Phys. B* **21** 066103
[17] Zhou Y Q and Stell G 1989 *Mol. Phys.* **66** 767
[18] Zhou Y Q and Stell G 1989 *Mol. Phys.* **66** 791
[19] Zhou Y Q and Stell G 1989 *Mol. Phys.* **68** 1265

[20] Frenkel D and Smit B 2002 *Understanding Molecular Simulation: from Algorithms to Applications* (London: Academic Press)
[21] Peterson B K and Gubbins K E 1987 *Mol. Phys.* **62** 215
[22] Magda J J, Tirrell M and Davis H T 1985 *J. Chem. Phys.* **83** 1888
[23] Li J, Wu K L, Chen Z X, Wang W Y, Yang B, Wang K, Luo J and Yu R J 2019 *Appl. Energy* **251** 113368
[24] Cui Z H, Fang H W, Huang L, Ni K and Reible D 2017 *J. Soils Sediments* **17** 2887
[25] Jagiello J, Kenvin J, Ania C O, Parra J B, Celzard A and Fierro V 2020 *Carbon* **160** 164
[26] Bojan M J and Steele W A 1988 *Surf. Sci.* **199** L395
[27] Schoen M and Diestler D J 1997 *Phys. Rev. E* **56** 4427
[28] Bock H and Schoen M 1999 *Phys. Rev. E* **59** 4122
[29] Diestler D J and Schoen M 2000 *Phys. Rev. E* **62** 6615
[30] Porcheron F, Schoen M and Fuchs A H 2002 *J. Chem. Phys.* **116** 5816
[31] Wu H, Borhan A and Fichthorn K A 2010 *J. Chem. Phys.* **133** 054704
[32] Shahraz A, Borhan A and Fichthorn K A 2012 *Langmuir* **28** 14227
[33] Liu L M, Zeng Y H, Do D D, Nicholson D and Liu J J 2018 *Adsorption* **24** 1
[34] Malijevsky A and Parry A O 2013 *J. Phys.: Condens. Matter* **25** 305005
[35] Malijevsky A 2014 *J. Phys.: Condens. Matter* **26** 315002
[36] Malijevsky A and Parry A O 2019 *Phys. Rev. E* **99** 042804
[37] Malijevsky A 2019 *Phys. Rev. E* **99** 040801(R)
[38] Malijevsky A and Parry A O 2014 *J. Phys.: Condens. Matter* **26** 355003
[39] Jagiello J and Olivier J P 2013 *Carbon* **55** 70
[40] Jagiello J and Jaroniec M 2018 *J. Colloid Interface Sci.* **532** 588
[41] Jagiello J and Kenvin J 2019 *J. Colloid Interface Sci.* **542** 151
[42] Yatsyshin P, Savva N and Kalliadasis S 2015 *J. Phys.: Condens. Matter* **27** 275104
[43] Yatsyshin P, Parry A O, Rascón C and Kalliadasis S 2018 *Mol. Phys.* **116** 1990
[44] Neimark A V, Lin Y, Ravikovitch P I and Thommes M 2009 *Carbon* **47** 1617
[45] Landers J, Gor G Y and Neimark A V 2013 *Colloids Surf. A Physicochem. Eng. Aspects* **437** 3
[46] Khlyupin A and Aslyamov T 2017 *J. Stat. Phys.* **167** 1519
[47] Khlyupin A and Aslyamov T 2021 *Phys. Rev. E* **103** 022104
[48] Forte E, Haslam A J, Jackson G and Müller E A 2014 *Phys. Chem. Chem. Phys.* **16** 19165
[49] Ravipati S, Galindo A, Jackson G and Haslam A J 2019 *Phys. Chem. Chem. Phys.* **21** 25558
[50] Shi K H, Santiso E E and Gubbins K E 2019 *Langmuir* **35** 5975
[51] Steele W A 1973 *Surf. Sci.* **36** 317
[52] Evans R 1979 *Adv. Phys.* **28** 143
[53] Barker J A and Henderson D 1967 *J. Chem. Phys.* **47** 4714
[54] Cotterman R L, Schwarz B J and Prausnitz J M 1986 *AIChE J.* **32** 1787
[55] Yu Y X and Wu J Z 2002 *J. Chem. Phys.* **117** 10156
[56] Sears M P and Frink L J D 2003 *J. Comput. Phys.* **190** 184
[57] Sauer E and Gross J 2017 *Ind. Eng. Chem. Res.* **56** 4119
[58] Yu Y X 2009 *J. Chem. Phys.* **131** 024704
[59] Peng B and Yu Y X 2008 *J. Phys. Chem. B* **112** 15407
[60] Liu Y, Liu H L, Hu Y and Jiang J W 2010 *J. Phys. Chem. B* **114** 2820
[61] Fu J, Liu Y, Tian Y and Wu J Z 2015 *J. Phys. Chem. C* **119** 5374
[62] Johnson J K, Zollweg J A and Gubbins K E 1993 *Mol. Phys.* **78** 591
[63] Carnahan N F and Starling K E 1969 *J. Chem. Phys.* **51** 635
[64] Sun Z L, Kang Y S and Kang Y M 2019 *Ind. Eng. Chem. Res.* **58** 15637
[65] Sun Z L, Kang Y S and Kang Y M 2019 *Chin. Phys. B* **28** 036102
[66] Snook I K and van Megen W 1980 *J. Chem. Phys.* **72** 2907
[67] Gardner L, Kruk M and Jaroniec M 2001 *J. Phys. Chem. B* **105** 12516
[68] Magda J J, Tirrell M and Davis H T 1985 *J. Chem. Phys.* **83** 1888
[69] Jagiello J, Ania C, Parra J B and Cook C 2015 *Carbon* **91** 330
[70] Balbuena P B, Berry D and Gubbins K E 1993 *J. Phys. Chem.* **97** 937
[71] Frink L J D and van Swol F 1998 *J. Chem. Phys.* **108** 5588
[72] Ghatak C and Ayappa K G 2004 *J. Chem. Phys.* **120** 9703
[73] Leroy F and Müller-Plathe F 2010 *J. Chem. Phys.* **133** 044110
[74] Evans R and Marconi U M B 1987 *J. Chem. Phys.* **86** 7138
[75] Quéré D 2008 *Annu. Rev. Mater. Res.* **38** 71
[76] Bridgman P W 1914 *Phys. Rev.* **3** 273
[77] Rowlinson J S and Swinton F L 1982 *Liquids and Liquid Mixtures* (London: Butterworth)
[78] Tang Y P and Lu B C Y 1997 *AIChE J.* **43** 2215
[79] Kolafa J and Nezbeda I 1994 *Fluid Phase Equilib.* **100** 1
[80] Mecke M, Müller A, Winkelmann J, Vrabec J, Fischer J, Span R and Wagner W 1996 *Int. J. Thermophys.* **17** 391